ADVANCED ENERGY MATERIALS
www.advenergymat.de

Screening and Development of Sacrificial Cathode Additives for Lithium-Ion Batteries

Haegyeom Kim, KyuJung Jun, Nathan Szymanski, Venkata Sai Avvaru, Zijian Cai, Matthew Crafton, Gi-Hyeok Lee, Stephen E. Trask, Finn Babbe, Young-Woon Byeon, Peichen Zhong, Donghun Lee, Byungchun Park, Wangmo Jung, Bryan D. McCloskey, and Wanli Yang*

This work presents a computational screening approach to identify Li-rich transition-metal oxide sacrificial cathode additives and provides experimental validation of antifluorite-structured Li_6MnO_4 as a potential candidate. Initial attempts to synthesize this compound result in low purity (≤40% by weight) owing to close thermodynamic competition with Li_2O and MnO at low temperature. However, it is shown that a much higher purity of 85% by weight can be achieved by combining Li excess with rapid cooling from high temperature, which effectively stabilizes the Li_6MnO_4 phase. The synthesized product delivers a high irreversible Li release capacity that exceeds 700 mAh g^{-1} by utilizing combined Mn oxidation ($Mn^{2+/3+}$ and $Mn^{3+/4+}$) and O oxidation. These results demonstrate that Li_6MnO_4 may therefore be useful as a potential sacrificial cathode additive in Li-ion batteries and motivate further investigation of other structurally-related compounds. While attempts were made to synthesize two additional compounds among computationally screened candidates, it was not successful to experimentally realize the two candidates. The difficulty of experimental realization of the newly predicted materials remains a challenge and it is suggested that more efforts need to be devoted to developing computational techniques to precisely predict synthesizability and propose potential synthetic routes of the predicted materials.

1. Introduction

The development of next-generation Li-ion batteries with improved energy density is pivotal to address the ever-increasing demand for electrochemical energy storage devices in various sectors, including electric transportation, portable devices, and grid-scale energy storage systems. A key remaining challenge is the low coulombic efficiency in the first few cycles, which largely stems from the formation of a solid electrolyte interphase (SEI). This issue becomes especially problematic when high-capacity alloying anode materials, such as Si or Sn, are added to the anode composite to increase the cell energy density. In this case, loss of accessible lithium in the cell is triggered, eventually reducing the total energy that the system can store during its operation.

Pre-lithiation has been suggested as a strategy to compensate for this

H. Kim, K. Jun, N. Szymanski, V. Sai Avvaru, Z. Cai, Y.-W. Byeon
Materials Sciences Division
Lawrence Berkeley National Laboratory
Berkeley, CA 94720, USA
E-mail: haegyumkim@lbl.gov
K. Jun, N. Szymanski, Z. Cai, P. Zhong
Department of Materials Science and Engineering
University of California
Berkeley, CA 94720, USA
M. Crafton, B. D. McCloskey
Department of Chemical and Biomolecular Engineering
University of California
Berkeley, CA 94720, USA
G.-H. Lee, W. Yang
Advanced Light Source
Lawrence Berkeley National Laboratory
Berkeley, CA 94720, USA
S. E. Trask
Chemical Sciences and Engineering Division
Argonne National Laboratory
Lemont, IL 60439, USA
F. Babbe
Chemical Sciences Division
Lawrence Berkeley National Laboratory
Berkeley, CA 94720, USA

The ORCID identification number(s) for the author(s) of this article can be found under https://doi.org/10.1002/aenm.202403946

DOI: 10.1002/aenm.202403946

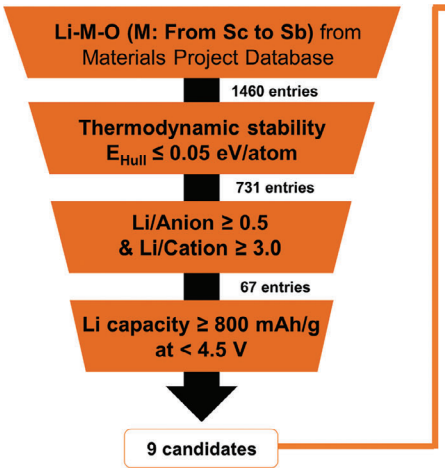

No.	Composition	Capacity (mAh/g at < 4.5V)	Oxidation State of M	M oxidation ability	E above Hull (meV/atom)	MP-ID
1	Li_8TiO_6	988	+4	N	4	772521
2	Li_8CrO_6	1033	+4	Y	36	756239
3	Li_6MnO_4	819	+2	Y	6	770533
4	$Li_{14}Mn_2O_9$	898	+2	Y	47	770530
5	Li_5NiO_4	835	+3	Y	11	771876
6	Li_6NiO_4	956	+2	Y	21	756411
7	Li_6ZnO_4	921	+2	N	0	14495
8	Li_8GeO_6	938	+4	N	1	28548
9	Li_8ZrO_6	866	+4	N	1	755225

Figure 1. Computational screening workflow used to identify promising sacrificial cathode additive candidates.

lithium loss by adding excess lithium to the anode or cathode.[1–4] Typical pre-lithiation methods include electrochemical pre-lithiation,[5,6] chemical pre-lithiation,[7] and the introduction of pre-lithiation additives to either the cathode[8,9] or anode.[10] Among these methods, pre-lithiation additives used in cathode composites have drawn significant attention because they avoid the challenges of handling highly reactive anode components[4,10,11] and require only a simple modification of the manufacturing process. A cathode pre-lithiation additive irreversibly releases lithium during the first charging process to compensate for the initial lithium loss, and the residue remains inactive in the cathode composite during the remaining life of the cell. As such, they are often referred to as sacrificial cathode additives.

An ideal sacrificial cathode additive irreversibly releases a large amount of lithium in the first charging process, and its residue remains stable during battery operation without causing any detrimental side reactions. Several high-lithium-content transition-metal oxides have been investigated as sacrificial cathode additives.[2,12] For example, antifluorite Li_5FeO_6 has been proposed as a viable candidate material[13–18] due to its low cost and high irreversible capacity. However, its poor stability in the air remains a problem. Another antifluorite-structured material Li_6CoO_4 has been widely investigated;[19–22] yet, the reactivity of its charging residue and the use of cobalt remain drawbacks. Other materials such as Li_2MoO_3,[23,24] Li_2CuO_2,[25,26] and Li_2NiO_2[27–30] have been investigated; however, they provide lower irreversible lithium release capacities than antifluorite compounds.

In this work, high-throughput computational screening is performed to identify promising candidates for sacrificial cathode additives. Antifluorite-structured Li_6MnO_4 is identified as a candidate material that uses inexpensive metal (Mn) while providing a high theoretical Li extraction capacity of 819 mAh g^{-1}. To investigate and optimize the synthesis of Li_6MnO_4, we use in situ X-ray diffraction (XRD) and density functional theory (DFT) calculations of reaction energies. Once synthesized with reasonably high purity, the Li extraction mechanism of Li_6MnO_4 is determined using X-ray absorption spectroscopy (XAS), resonant inelastic X-ray scattering (RIXS), and differential electrochemical mass spectrometry (DEMS). Our work showcases the effectiveness of Li_6MnO_4 as a sacrificial cathode additive, motivating future investigation into this compound and other structurally related materials identified using computations.

2. Results

2.1. Computational Screening of Promising Sacrificial Cathode Additives

Sacrificial cathode additive candidates were computationally screened from the Materials Project (MP) database using the workflow outlined in **Figure 1**. We only considered Li-containing ternary metal oxides (Li–*M*–O), where the metal (*M*) species included elements with atomic numbers ranging from 21 (Sc) to 51 (Sb). These oxides were filtered to exclude any compounds whose energy above the convex hull is greater than 50 meV $atom^{-1}$ at 0 K, as these compounds are unlikely to be synthesizable experimentally.[31] The magnitude of the energy above the convex hull corresponds to the driving force to decompose to the lowest-energy phases in the given phase diagram and is a measure of the thermodynamic stability of a compound with respect to the ground-state competing phases. From the resulting compounds, we selected those with a high Li/anion ratio (≥0.5) and a high Li/M ratio (≥3.0) as potential sacrificial cathode additives, as these materials could hypothetically deliver a high specific capacity through the extraction of their Li in the first charging process. This process produced a list of 67 compounds, for which the voltage curves were evaluated using DFT calculations performed on topotactically delithiated versions of the host structures (see Experimental Section). We used a high-voltage criterion because

D. Lee, B. Park
Advanced Cell Research Center
LG Energy Solution
Daejeon 34122, Republic of Korea
W. Jung
Development Procurement Department
LG Energy Solution
Daejeon 34122, Republic of Korea

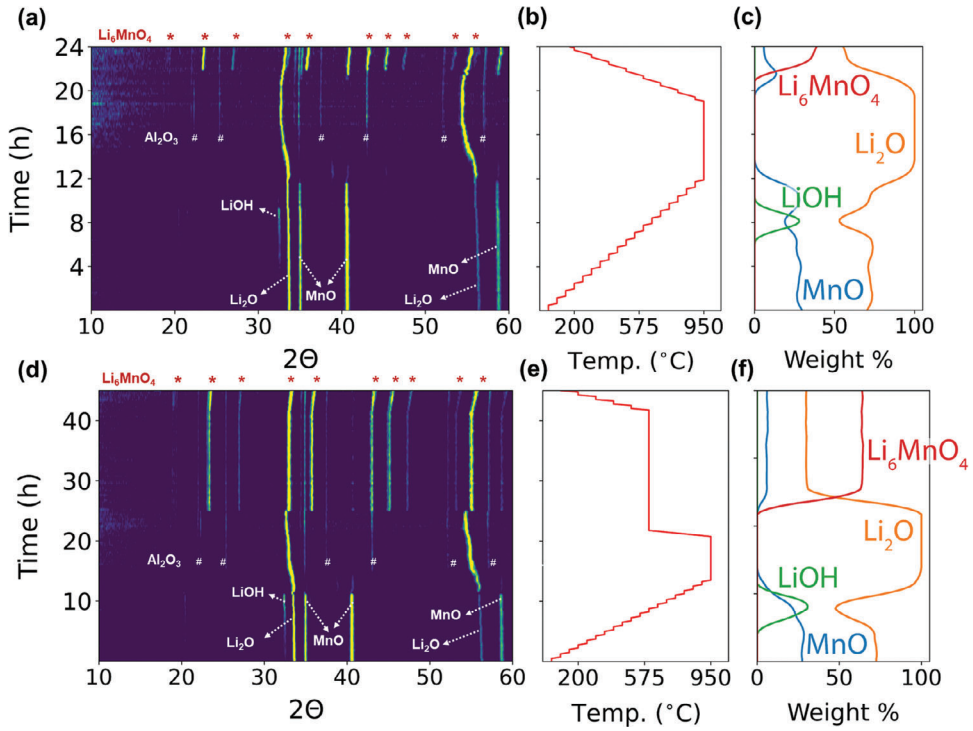

Figure 2. In situ characterization of Li_6MnO_4 synthesis. a) Heatmap showing XRD intensities collected from a sample of Li_2O and MnO that was heated to 950 °C and slowly cooled to synthesize Li_6MnO_4. b) Heating profile associated with the experiment shown in panel (a). c) Weight fractions obtained from the XRD measurements shown in panel (a). d) Heatmap showing the XRD intensities collected from a sample of Li_2O and MnO, which was heated to 950 °C, rapidly cooled to 600 °C, and held for 20 h before letting the sample slowly cool to room temperature. e) Heating profile associated with the experiment shown in panel (d). f) Weight fractions obtained from the XRD measurements shown in panel (d).

our computed voltage profiles only consider topotactic delithiation pathways, which may overestimate the lithium extraction potential if the delithiation products are highly unstable and conversion reactions are more favorable. A final selection criterion was then imposed whereby compounds with a predicted capacity exceeding 800 mAh g^{-1} at voltages $\leq$ 4.5 V (vs Li/Li^+) were identified. These compounds include Li_8TiO_6, Li_8CrO_6, Li_6MnO_4, $Li_{14}Mn_2O_9$, Li_5NiO_4, Li_6NiO_4, Li_6ZnO_4, Li_8GeO_6, and Li_8ZrO_6. Additional information (e.g., predicted capacity) on each of these compounds is provided in Figure 1. Of these nine candidates, we selected Li_6MnO_4 for experimental investigation for several reasons: i) it does not contain any critical elements such as Ni and Co, instead relying on Mn that is much more abundant; ii) it can potentially use "two-electron transfer" (or "double redox": $Mn^{2+/3+}$ and $Mn^{3+/4+}$), which can provide high theoretical capacity without requiring detrimental oxygen oxidation; and iii) it is close (6 meV $atom^{-1}$) to the convex hull, suggesting that experimental synthesis may be viable.

2.2. Understanding Li_6MnO_4 Synthesis Mechanisms

The first synthesis of Li_6MnO_4 was reported by Narukawa et al.,[20] who mixed Li_2O and MnO in a 3:1 ratio and heated the sample at 950 °C for 12 h under a reducing atmosphere (99% N_2, 1% H_2) before letting it cool naturally to room temperature. Despite the reported success of this synthesis procedure, the XRD pattern acquired from its product deviates from that anticipated for Li_6MnO_4 (mp-770533 in the MP database), suggesting that prominent impurities may be present. Later work by Szymanski et al.[32] reaffirmed the presence of substantial impurity peaks that arise from an attempted synthesis of Li_6MnO_4.

To better understand how Li_6MnO_4 forms during solid-state synthesis and to identify the secondary phases that limit its purity, we performed in situ XRD measurements on a precursor mixture of Li_2O and MnO that was heated to 950 °C, held for 8 h, and cooled to room temperature under a reducing atmosphere (98% Ar, 2% H_2). Experimental details of the in situ XRD characterization can be found in the experimental section. **Figure** 2a–c shows the phase transformation observed during this synthesis process. We find that Li_2O does not react with MnO at temperatures below 900 °C, although a small amount of LiOH temporarily forms due to the presence of H_2 in the reducing atmosphere. Interestingly, above 900 °C, we found two noticeable changes in the XRD patterns: i) the diffraction peaks associated with MnO disappear and ii) the peaks associated with Li_2O undergo a prominent shift toward lower 2θ, consistent with lattice expansion. The simultaneous occurrence of these two changes suggests the incorporation of the larger Mn^{2+} ions (66 pm) into the antifluorite structure of Li_2O (where Li^+ has a smaller ionic radius of 59 pm). Indeed, our DFT calculations and Monte Carlo simulations indicate that it is thermodynamically favorable for tetrahedral cations in Li_6MnO_4 to disorder above ≈700 °C (Figure S1, Supporting Information). The presence of a disordered Li_6MnO_4 phase at high temperatures is further evidenced by the fact that the ordered version of this phase appears during cooling ($\lesssim$ 600 °C). However,

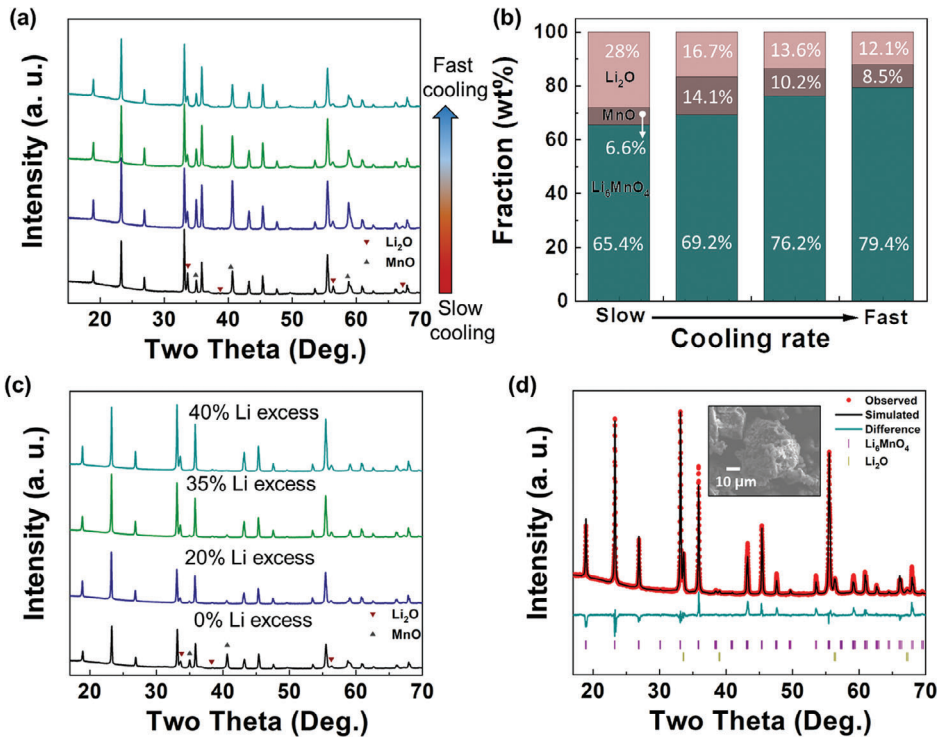

Figure 3. Structure characterization of synthesized Li_6MnO_4 under varied conditions. a) XRD patterns of the synthesized Li_6MnO_4 with varied cooling rates and b) corresponding weight fraction analysis of Li_6MnO_4, Li_2O, and MnO. c) XRD patterns of the synthesized Li_6MnO_4 at varied Li_2O:MnO ratios (varied Li excess level). d) Rietveld refinement result of Li_6MnO_4 synthesized with 40% Li excess using X'Pert Highscore Plus. Inset: SEM image of synthesized Li_6MnO_4.

the formation of ordered Li_6MnO_4 is accompanied by its partial decomposition into MnO and Li_2O. As a result, the final product contained only ≈40% Li_6MnO_4 by weight.

To improve the purity of Li_6MnO_4 in its ordered configuration, we performed a second experiment where the sample was rapidly cooled from 950 to 600 °C and held for 20 h before being slowly cooled to room temperature. The XRD patterns collected during this synthesis experiment are presented in Figure 2d–f, revealing an increased yield of ordered Li_6MnO_4 that reaches 65 wt.% by the end of cooling. These results suggest that Li_6MnO_4 is only stable at high temperature, and therefore, rapid cooling is needed to avoid (or at least minimize) its decomposition into Li_2O and MnO. From DFT calculations reported in the MP, Li_6MnO_4 is indeed metastable at 0 K, with an energy of 6 meV atom^{-1} above the convex hull. However, configurational disorder on cation sites in Li_6MnO_4 can significantly lower its free energy at high temperature — on the order of 100 meV atom^{-1}, as shown in Figure S1 (Supporting Information) — thereby stabilizing this phase relative to Li_2O and MnO. To capitalize on the stability of Li_6MnO_4 that occurs at high temperature while retaining it at low temperature, we further investigate the effectiveness of fast cooling in the next section.

2.3. Synthesis Optimization of Li_6MnO_4

To examine the impact of the cooling rate on the purity of Li_6MnO_4, in **Figure** 3a, we present XRD patterns obtained from reaction products of Li_2O and MnO when held at 950 °C for 12 h under a continuous flow of the mixed gas (98% Ar, 2% H_2) but with varied cooling rates. The ratios of Li_2O and MnO were kept fixed at 3:1 for all these experiments. For the slowest cooling, we simply turned off the furnace after the completion of the 12-h dwell time (black line). To slightly increase the cooling rate, we turned off the furnace and opened the insulating cover immediately after the dwell (blue line). To accelerate the cooling rate further, we removed the furnace's tube from the heating element and let it cool down while retaining a gas flow through it (green line). We retained the gas flow during the cooling to avoid any potential oxidation of Mn and unwanted side reactions upon air exposure. The fastest cooling was achieved by applying a cooling fan to the furnace's tube that was removed from the heating element (dark cyan line). From the XRD analysis, the purity of Li_6MnO_4 is found to increase substantially with faster cooling rates. This result is clearly evidenced by the prominent decrease in the peak intensity of the Li_2O and MnO impurities. Figure 3b shows the refined weight fraction of Li_6MnO_4 in the samples obtained using varied cooling rates (see the refinement results in Figure S2, Supporting Information). The weight fraction of Li_6MnO_4 increases from ≈65% to ≈80% by weight. However, even with the fastest cooling rate, some Li_2O and MnO impurities still persist.

To further improve the purity of Li_6MnO_4, we tested the use of excess Li_2O precursor. In these experiments, we applied the fastest cooling rate described above. This is anticipated to be beneficial to increase reactive interfaces between MnO and Li_2O, allowing all the MnO particles to react to form Li_6MnO_4. We

expect any unreacted Li_2O could be evaporated during the high-temperature synthesis process. In addition, some Li_2O residues might be lost in the washing procedure used after synthesis (described later in this section) in an attempt to purify the sample. Figure 3c presents the XRD patterns of samples synthesized with varied amounts of Li excess. With increasing levels of Li excess in the precursor mixture, the resulting product shows a decrease in the amount of MnO that is present. The peaks associated with MnO are completely undetectable once the Li-excess level reaches 40% (i.e., when the ratio of Li_2O to MnO is 4.2). Nevertheless, substantial amounts of the unreacted Li_2O impurity remain after each synthesis attempt. The Li_6MnO_4 synthesized with 40% Li excess was subjected to phase quantification using Rietveld refinement using X'Pert Highscore Plus as shown in Figure 3d. For the Rietveld refinement, crystal structure data of Li_6MnO_4 (mp-770533, space group: $P4_2/nmc$) was obtained from the MP database. This refinement suggests a weight fraction of 85.4% for Li_6MnO_4 (with lattice parameters $a = 6.632$ Å, $b = 6.625$ Å, and $c = 4.670$ Å), which coexists with 14.6 wt.% Li_2O. Because our synthetic method cannot control the cooling rate precisely, we tested the reproducibility of our synthesis process. In the optimized synthesis condition, the purity of Li_6MnO_4 was 84.5±1.0 wt.%. The inset of Figure 3d shows a scanning electron microscopy (SEM) image acquired from presumed Li_6MnO_4 particles in the sample, where 2–3 µm primary particles are agglomerated to form a ≈40 µm secondary particle. To quantify the composition of the sample, we performed inductively coupled plasma mass spectrometry (ICP-MS) measurements, revealing a Li:Mn ratio of 8.5:1, which is close to the Li:Mn ratio in the precursor mixture. This result indicates that almost no Li has evaporated during the synthesis process. Given the overall sample composition and the weight fraction of each identified phase, we can denote the final synthesis product as $Li_6MnO_4 \cdot \alpha Li_2O$ ($\alpha < 1.25$). In an attempt to remove the Li_2O impurity, we washed the sample with water after synthesis. Unfortunately, it appears that Li_6MnO_4 is unstable in contact with water as it is found to completely transform into $LiMn_2O_4$ after the washing procedure (Figure S3, Supporting Information). Nevertheless, the purity of Li_6MnO_4 obtained in this study is still reasonably high, which allows us to investigate its intrinsic electrochemical properties and delithiation mechanisms as a potential artificial cathode additive for the first time in the following section.

2.4. Li Extraction Mechanisms

We investigated the Li extraction mechanisms of Li_6MnO_4 using in situ electrochemistry-XRD analysis. **Figure 4a** shows the XRD patterns acquired during the charge and discharge of the synthesis product that shows the highest purity (85.4 wt.%) of Li_6MnO_4. Figure 4b displays charge–discharge profiles measured from this sample, with a current density of 5 mA g^{-1} in the voltage range of 4.5–2.5 V (vs Li/Li^+). During the charging process, we do not observe any prominent changes in the peak positions of the XRD patterns. This result agrees with the previous report by Narukawa et al.[20] They also found no change in the peak positions of Li_6MnO_4 after 0.25 Li ions were extracted, which led to the conclusion that Li cannot be extracted

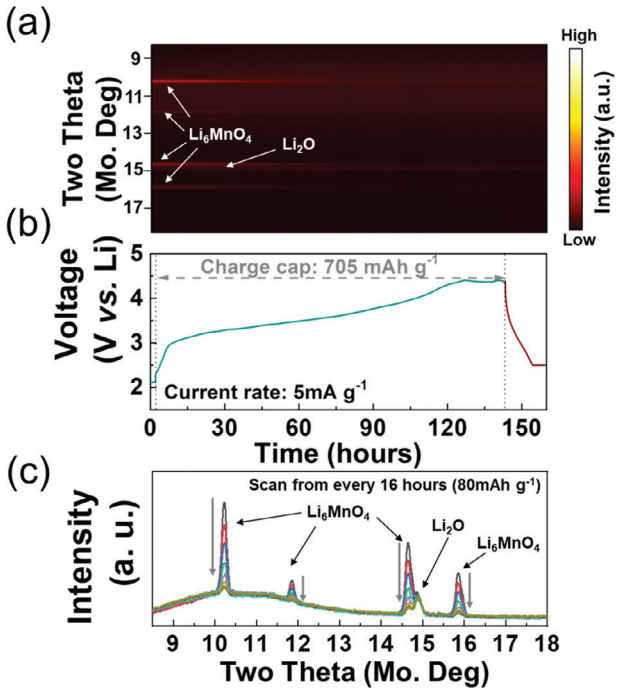

Figure 4. In situ electrochemistry-XRD characterization. a) XRD heat maps of Li_6MnO_4 during charging and b) associated charge–discharge profiles at 5 mA g^{-1}. c) XRD patterns of Li_6MnO_4 during charging. Scan from every 16 h (80 mAh g^{-1}).

from the compound at reasonable voltages. However, we found that the peak intensity associated with Li_6MnO_4 does continuously decrease during the charging process. This is more clearly illustrated in Figure 4c, which shows that the peak intensity of Li_6MnO_4 linearly decreases as a function of charging state. These results suggest that Li_6MnO_4 may become amorphous or poorly crystalline upon delithiation. Importantly, we also found that Li_2O remains unchanged in XRD, both in terms of peak intensity and position, throughout the charging process, indicating all the observed charge capacity is derived from Li_6MnO_4. The total charge capacity of Li_6MnO_4 is found to be 705 mAh g^{-1}, corresponding to the extraction of ≈5 Li ions per formula unit.

A similar amorphization was observed in Li_6CoO_4 during the delithiation process by Jun et al. and Cui et al.[21,33] Their studies did not observe a noticeable peak shift during the delithiation from the Li_6CoO_4 phase, but the XRD peaks from Li_6CoO_4 completely disappeared when more than 2 Li ions per formula unit were extracted. In the case of another sacrificial cathode additive, Li_5FeO_4, the structure was destroyed and transformed into a disordered rocksalt phase when 2 Li ions per formula unit were removed.[14] In contrast, while the peak intensities of Li_6MnO_4 gradually decreased, they did not completely disappear nor convert into the disordered rocksalt phase until 5 Li ions per formula unit were removed.

Interestingly, the Li_6MnO_4 exhibits a non-negligible discharge capacity (≈60 mAh g^{-1}). We suspect that the amorphous phase uptakes little Li ions during the discharging process. To understand whether the discharge capacity comes from the reduction of transition metal (i.e., Mn^{3+} to Mn^{2+}), we employed ex situ X-ray

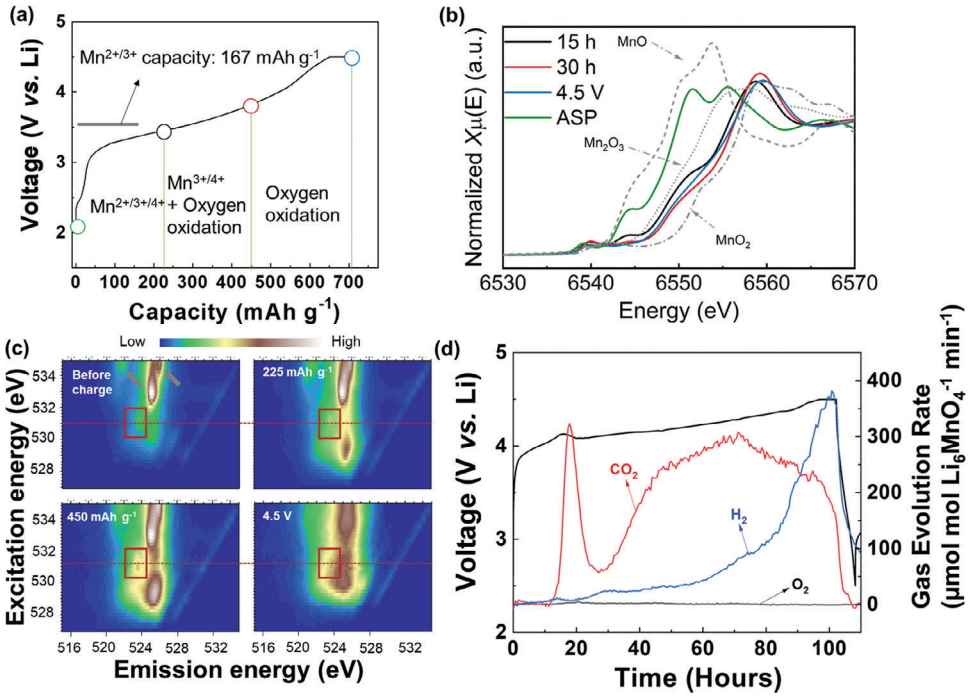

Figure 5. Characterization of Li_6MnO_4 during charging process. a) First charge profile of Li_6MnO_4 at 10 mA g^{-1}. b) Ex situ XANES analysis (Mn K-edge) of Li_6MnO_4 electrodes at varied charged states. c) O-*K* mapping of mRIXS of Li_6MnO_4 electrodes at varied charged states. d) DEMS analysis results of Li_6MnO_4 electrode at 10 mA g^{-1}.

photoelectron spectroscopy (XPS) technique as shown in Figure S4 (Supporting Information). After charging up to 4.5 V, Mn *2p* peak shifts to higher binding energy, indicating oxidation. However, the discharging to 2.5 V does not shift the Mn 2p peak to lower binding energy. This result confirms that the Mn is not reversibly reduced upon discharging. Therefore, it is highly likely that the discharge capacity is attributable to capacitive reactions.

To better understand the Li extraction reaction mechanisms of Li_6MnO_4, we employed ex situ bulk sensitive hard X-ray absorption near-edge structure (XANES) analysis. In **Figure** 5a,b, we compare the Mn K-edge spectra at different states of charge with MnO (Mn^{2+}), Mn_2O_3 (Mn^{3+}), and MnO_2 (Mn^{4+}) references. In the as-prepared pristine (ASP) sample, the Mn valence is close to +2, which is consistent with the Li_6MnO_4 chemical formula. Upon charging to 225 mAh g^{-1}, the Mn K-edge shifts to higher energy and slightly bypasses the Mn_2O_3 reference. This observation indicates that the oxidation state of Mn increases up to > +3. Charging to 450 mAh g^{-1} further oxidizes the Mn, as evidenced by the Mn K-edge shift; however, the valence does not reach +4. When charged up to 4.5 V, the Mn K-edge slightly shifts to lower energy, which is related to the complicated redox coupling phenomenon between the O and Mn oxidation process at high voltage.[34,35] This phenomenon indicates that Mn oxidation is not the only active redox mechanism and that oxygen oxidation may play a role.

Figure 5c demonstrates the O-*K* mapping of resonant inelastic X-ray scattering (mRIXS) to identify the contribution of oxygen oxidation in the Li-extraction process. In the O-*K* mapping, brown indicates higher intensity whereas blue shows lower intensity. The strong features at 525/534 and 522/534 of emission energy/excitation energy (highlighted by grey arrows) likely indicate the presence of Li_2CO_3.[36] As we did not observe any crystalline Li_2CO_3 in the XRD analysis, it is expected that a poorly crystalline or amorphous Li_2CO_3 is present in the sample. When charging up to 450 mAh g^{-1}, these features weaken, indicating the decomposition of Li_2CO_3. More importantly, the feature highlighted by the red box originates from oxidized oxygen species. The emergence of such a feature again indicates the oxygen oxidation to compensate for the Li extraction. As shown in Figure 5c, the intensity of the oxidized oxygen feature starts to increase when the cathode is charged to 225 mAh g^{-1}, and the relative intensity of this feature is enhanced upon further oxidation up to 450 mAh g^{-1}. However, at the 4.5-V charged state, we no longer observe the oxidized oxygen feature, and pre-edge features near ≈528 eV of excitation energy show a noticeable change, which suggests that the subsurface electronic structure is completely changed. This finding is in agreement with the completely diminished XRD peaks of Li_6MnO_4 after fully charging up to 4.5 V (Figure 4).

Differential electrochemical mass spectrometry (DEMS) was employed to investigate outgassing during the cycling of Li_6MnO_4 as shown in Figure 5d. Large amounts of CO_2 and H_2 evolution were observed during the first charge, whereas no O_2 evolution was detected. The CO_2 evolution observed during the first charge occurs in two distinct peaks, including one relatively sharp peak occurring early during charging and a broader peak occurring over the latter portion of the first charge. The H_2 evolution occurs as a single peak that slowly grows over the course of the first charge and reaches a maximum at the end of the charge. CO_2 may arise due to the decomposition of native

carbonate species (such as Li_2CO_3) on the surface of Li_6MnO_4 or the decomposition of the carbonate solvents in the electrolyte.[37] In particular, given that the Li_2CO_3 feature disappeared during the initial charging process in the mRIXS analysis, the CO_2 evolution during the earlier charging process with the relatively sharp peak can likely be attributed to the decomposition of Li_2CO_3. In contrast, H_2 evolution may result from an electrode crosstalk process in which electrolyte degradation at the Li_6MnO_4 surface generates protic electrolyte degradation products, which are subsequently reduced at the anode surface to form H_2.[38] Although the mechanism underlying the electrolyte degradation that is responsible for much of the observed outgassing is unclear, it is likely that the interfacial reactivity of the Li_6MnO_4 is at least elevated due to the large amounts of anion redox occurring within the material. For example, the electrolyte degradation may be initiated by a reaction of the electrolyte solvent with reactive oxidized oxygen species formed during the charging of Li_6MnO_4. Although direct O_2 evolution is not observed, other oxidized oxygen species may be formed that subsequently react with the electrolyte and produce CO_2.[21] The gas evolution from the lattice creates cracks in the Li_6MnO_4 particles as shown in SEM analysis (Figure S5, Supporting Information).

2.5. Stability of Li_6MnO_4 in Ambient Air

We evaluated the air stability of Li_6MnO_4. Figure S6a (Supporting Information) shows XRD patterns of Li_6MnO_4 electrodes before and after air exposure (24 h). A peak located at ≈18° is originated from PTFE binder used for the electrode preparation.[39] After the air exposure for 24 h, the peak intensity of Li_6MnO_4 significantly decreases and new diffraction peaks appear. The new peaks evolved after the air exposure are well matched with Li_2CO_3 phase. We expect that Li ions are removed from Li_6MnO_4 and it forms Li_2CO_3 by reacting with CO_2 in the air. Figure S6b (Supporting Information) shows the charge–discharge profiles of Li_6MnO_4 after air exposure (24 h). After the air exposure, Li_6MnO_4 could not be charged and exhibited a low charge capacity of ≈20 mAh g^{-1}. These results indicate instability of Li_6MnO_4 in ambient air. Improving its stability upon air exposure could be an important future research direction.

2.6. Effect of Li_6MnO_4 Additive in Full Cells

To evaluate the effect of Li_6MnO_4 as a sacrificial cathode additive, we constructed and tested full cells with and without Li_6MnO_4. In this system, we used $LiNi_{0.8}Mn_{0.1}Co_{0.1}O_2$ (NMC811) as a cathode active material and SiO_x-graphite composite as an anode active material. For the sample with Li_6MnO_4 additive, we mixed NMC811 and Li_6MnO_4 in a 9:1 ratio in mass (10 wt.% of Li_6MnO_4 additive). First, we tested NMC811 cathode and NMC811 with Li_6MnO_4 additive in a Li metal half-cell. **Figure 6**a,b exhibit charge–discharge profiles of NMC811 without Li_6MnO_4 additive and NMC811 with Li_6MnO_4 additive, respectively, at 30 mA g^{-1}. NMC811 cathode delivers 251.9 and 225.8 mAh g^{-1} for the first charge and discharge, respectively. The initial coulombic efficiency (ICE) is ≈89.6% for NMC811. When 10 wt.% of Li_6MnO_4 additive is used, the cathode shows 264.4 mAg $^{-1}$ for the first charge and 202.2 mAh g^{-1} for the first discharge, exhibiting 76.5% of ICE. When the discharge capacity is re-calculated based on the NMC811 mass only, it becomes 224.7 mAh g^{-1}, which is close to the value obtained by NMC811 only. This result demonstrates that Li_6MnO_4 contributes to the charge capacity only as a sacrificial cathode additive. We used the SiO_x-graphite composite as an anode and tested the composite anode in a Li metal half-cell. Figure 6c shows the initial two charge–discharge cycles of the SiO_x-graphite composite anode at 250 mA g^{-1}. The SiO_x-graphite composite anode exhibits 2114.7 mAh g^{-1} of the first discharge capacity and 1493.7 mAh g^{-1} of the first charge capacity with ICE of 70.6%.

Finally, we assembled full cells by combining NMC811 cathode without Li_6MnO_4 additive or NMC811 with Li_6MnO_4 additive and the SiO_x-graphite composite anode. In our experiment, N/P ratio is fixed to be 1.0 based on the first charge capacity of the cathode and the first discharge capacity of the anode. Figure 6d,e shows the charge–discharge profiles of the full cells with NMC811 without Li_6MnO_4 additive and NMC811 with Li_6MnO_4 additive, respectively, at 30 mA $g^{-1}_{cathode}$. The full cell with Li_6MnO_4 additive delivers 175 mAh g^{-1}, which is slightly higher than the cell without additive (167 mAh g^{-1}). When the discharge capacity is re-calculated based on the NMC811 mass only for the cell with Li_6MnO_4 additive, it becomes 194.4 mAh g^{-1}, indicating higher utilization of NMC811. Figure 6f shows the cycling stability of the full cells with and without Li_6MnO_4 additive. Notably, the cell with Li_6MnO_4 additive exhibits improved cycling performance compared to the control group. This result highlights the effectiveness of our Li_6MnO_4 as a sacrificial cathode additive.

3. Discussion

In this study, we performed a computational screening for sacrificial cathode additives for Li-ion batteries. Li_6MnO_4 was identified as a potential sacrificial cathode additive with inexpensive metal price and high capacity. Although Li_6MnO_4 has previously been synthesized,[20,32] the synthesis product contained substantial amounts of Li_2O and MnO impurities. Our study demonstrates that rapid cooling and Li excess in the precursor mixture lead to increased purity of Li_6MnO_4 (up to ≈85% by weight), accompanied by a Li_2O impurity. Our calculations indicate that rapid cooling is needed because Li_6MnO_4 is metastable with respect to decomposition at room temperature. It is not yet fully understood why Li excess is needed to improve the purity of Li_6MnO_4; however, we speculate that it promotes reactivity between the precursors (Li_2O and MnO) at low temperature owing to the high mobility of Li ions.

During the charging process of Li_6MnO_4, oxygen oxidation was clearly observed by mRIXS analysis, particularly at 450 mAh g^{-1} of charged capacity; however, this feature disappeared at the top of charge (4.5 V vs Li/Li^+). This result likely indicates the irreversible oxygen loss (e.g., O_2 gas formation) from the crystalline Li_6MnO_4. However, DEMS analysis does not show any noticeable O_2 evolution during the charging process. Instead, a substantial amount of CO_2 evolution was confirmed. As the CO_2 evolution can originate from various reasons, it is difficult to pinpoint the origin of CO_2 evolution. However, we suggest that any oxidized

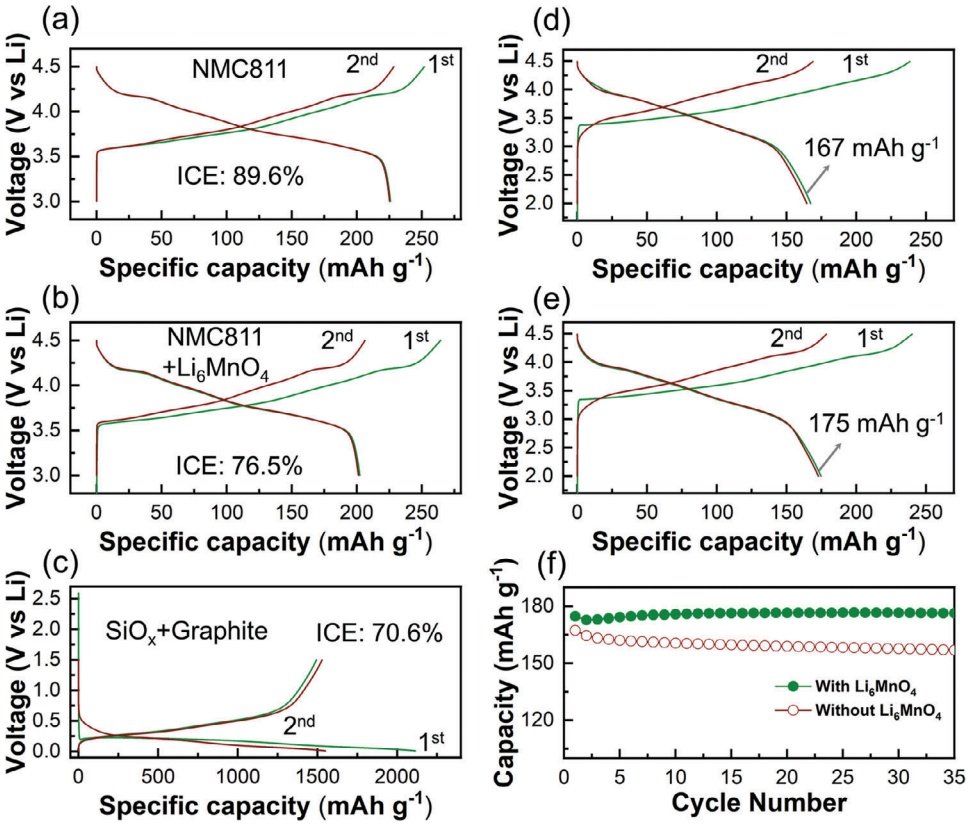

Figure 6. Electrochemical properties of cells with Li_6MnO_4 additive. Charge–discharge profiles of a) NMC811 cathode and b) NMC811 with Li_6MnO_4 additive in a Li metal half-cell. c) Charge–discharge profiles of the SiO_x-graphite composite anode in a Li metal half-cell. Charge–discharge profiles of d) NMC811 cathode and e) NMC811 with Li_6MnO_4 additive in a full-cell with the SiO_x-graphite composite anode. f) Cycling performance of the full cells with and without Li_6MnO_4 additive.

oxygen species formed during charging may react with the electrolyte or carbon additive to form CO_2.[40–42]

We further expanded our experimental efforts to synthesize two additional sacrificial cathode additives among the computationally predicted candidates. We selected two candidates, Li_8TiO_6 and Li_6NiO_4. Figure S7 (Supporting Information) shows XRD patterns of the synthesized products at varied synthetic conditions for the target of Li_8TiO_6 and Li_6NiO_4. For the synthesis of Li_8TiO_6, we controlled precursor selection, synthesis temperature, and Li excess composition. However, the synthesis produced Li_4TiO_4 with Li_2O impurities. When the synthesis temperature reached 1100 °C, the sample was completely melted. We expect that the Li_4TiO_4 phase is too stable to transform into the metastable Li_8TiO_6 phase. Table S1 (Supporting Information) summarizes the synthesis conditions and products for the Li_8TiO_6 target. For the synthesis of Li_6NiO_4, we selected Li_2O and NiO as precursors and controlled synthesis temperatures and reaction environments. Figure S7b (Supporting Information) shows XRD patterns of representative synthesis results of Li_6NiO_4 and Table S2 (Supporting Information) summarizes the synthesis conditions and products for the Li_6NiO_4 target. No chemical reactions were observed in the Ar flow conditions up to 1100 °C. When the synthesis temperature increased up to 1100 °C, the sample was completely melted. On the other hand, a NiO precursor was completely reduced to Ni metal in the H_2/Ar mixture gas flow conditions up to 1000 °C. At 1100 °C under the H_2/Ar mixture gas flow, an impurity of Li_5AlO_4 was found. We suspect that the alumina boat reacted with the Li_2O precursor. The difficulty synthesizing Li_6NiO_4 likely originated from its high metastability (energy above Hull: 21 meV atom^{-1}). While computational screening is useful for selecting promising candidate materials to some extent, it is often challenging to experimentally realize the predicted materials as demonstrated in our study. In particular, predicting the synthesizability of new compounds remains a big hurdle to overcome. More efforts need to be devoted to developing computational techniques to precisely predict synthesizability.

4. Conclusion

Our work suggests several lithium-rich transition-metal-oxide sacrificial cathode additives through computational screening and experimentally validates one candidate, antifluorite-structured Li_6MnO_4. We discovered that the cooling rate and Li excess in the precursor mixture play key roles in improving the purity of Li_6MnO_4 synthesis. Through synthesis condition optimization, this work improves the Li_6MnO_4 purity up to ≈85 wt.% with Li_2O impurity. The synthesized Li_6MnO_4 delivered an irreversible Li release capacity of > 700 mAh g^{-1} by utilizing $Mn^{2+/3+}$ and $Mn^{3+/4+}$ as well as oxygen oxidation, indicating the

potential of Li_6MnO_4 as a sacrificial cathode additive. Finally, we evaluated the Li_6MnO_4 additive in a full-cell system, which showed improved electrochemical performance compared to the control group without Li_6MnO_4 additive.

5. Experimental Section

Computation Details: *DFT calculations*: The DFT calculations were performed within the projector augmented wave formalism and generalized gradient approximation (GGA)[43] functional as implemented in the Vienna ab-initio simulation package.[44] An energy cutoff value of 520 eV was used. The electronic self-consistent loop and ionic relaxation loop were converged up to 10^{-6} and 10^{-5} eV, respectively. For each candidate compound, the total energy of each unit cell was computed after removing lithium one by one until all lithium was removed from the structure. For each lithium concentration, DFT calculations were performed for three Li-vacancy enumerations with the lowest Ewald energy[45] and used the lowest DFT energy structure to build the topotactic voltage profile. Calculation of the topotactic voltage profiles for the high-throughput screening was performed after applying the mixing scheme of GGA/GGA+U.[46]

Cluster-expansion Monte Carlo: The cluster expansion (CE) method and Monte Carlo method were used to investigate the configurational thermodynamics of Li_6MnO_4, where the cation sites can be occupied by Li^+/Mn^{2+}/vacancy. The CE expands the energy of multicomponent disordered materials as a sum of many-body configurational interactions:

$$E(\sigma) = J_0 + \sum_i J_i\sigma_i + \sum_{i,j} J_{ij}\sigma_i\sigma_j + \sum_{i,j,k} J_{ijk}\sigma_i\sigma_j\sigma_k + \cdots \quad (1)$$

where σ_i is the occupancy of different species (indicator basis site function) and J refers to the effective cluster interaction (ECI) using the indicator basis.[47] A CE Hamiltonian was fitted using a training set containing 132 Li_6MnO_4 structures with distinct orderings. The CE was constructed with pair interactions up to 7 Å, triplet interactions up to 4 Å, and quadruplet interactions up to 4 Å based on the unit cell of the Li_2O structure with lattice parameter a = 4.659 Å. In total, 84 ECIs, including the constant term J_0, were defined and fitted with energies calculated by r^{2}SCAN-DFT using an $\ell_0\ell_2$-norm regularized regression.[48] Readers are referred to the article by Barroso–Luque et al.[49] for details of CE fitting in ionic systems. To simulate atomic orderings at equilibrium, canonical Monte Carlo simulation was used with the Metropolis–Hastings algorithm. Overall, 1000 representative supercell structures ($Li_{1152}Mn_{192}O_{768}$) were sampled from the equilibrium ensemble to evaluate the average potential energy $E(T)$ at finite temperatures. The free energy to form Li_6MnO_4 was computed as a relative value with respect to the 0 K configuration using $\Delta G(T) = E(T) - TS(T)$, where the configurational entropy $S(T) = \int_0^T C_v(T)/T'dT'$ (C_v is the heat capacity) was calculated as an integral from the ordered Li_6MnO_4 configuration at 0 K. *Smol* was used for the Monte Carlo simulations[50] and *pymatgen* for the structure processing.[51]

Synthesis of Li_6MnO_4: Li_2O (Alfa Aesar, 99.5%) and MnO (Alfa Aesar, 99.9%) were homogeneously mixed by using a planetary ball mill (PM200, Retsch) at 250 rpm for 4 h. The ball-milling jar was sealed in an Ar-filled glovebox to avoid air exposure of the powder. The mixture was pelletized with a mold with 12-mm diameter. The pelletized samples were annealed to form the target phase at 950 °C for 12 h under a continuous flow of the mixed gas (98% Ar, 2% H_2), followed by different cooling processes.

Characterization of Li_6MnO_4: XRD analysis was conducted using a Rigaku Miniflex 600 equipped with a Cu Kα radiation source. The surface morphology and microstructure of the samples were examined using SEM (FEI Quanta FEG-250).

Electrochemistry: For the cathode film, Li_6MnO_4 powder (70 wt.%), super C65 carbon black (Timcal, 20wt.%)), and polytetrafluoroethylene (PTFE, DuPont, Teflon 8A, 10 wt.%) were homogeneously mixed with a mortar and pestle. The mixed composite was then rolled into free-standing thin films inside an Ar-filled glovebox. Coin-type 2032 two electrode cells were fabricated using the composite electrode (5/16-inch diameter) containing ≈7 mg cm^{-2} of the active material, Li-foil (FMC) counter/reference electrode, and a glass fiber separator (Whatman, GF/D type). The electrolyte consisted of a 1 M solution (99.99%, Solvionic) of $LiPF_6$ in a 1:1 mixture of ethylene carbonate (EC) and dimethyl carbonate (DMC). A glove box (mBraun) filled with high-purity argon (99.999%) and equipped with oxygen and moisture sensors/absorbers (H_2O and O_2 content < 1 ppm) was used for assembling the electrochemical cells. Li-ion half-cells were subjected to galvanostatic cycling at 10 mA g^{-1} using an Arbin battery test instrument for ex situ samples.

For the full-cell testing, $LiNi_{0.8}Mn_{0.1}Co_{0.1}O_2$ (NMC811; MSE supplies) without Li_6MnO_4 additive or NMC811 with 10 wt.% of Li_6MnO_4 additive was mixed with super C65 carbon black (Timcal), and polytetrafluoroethylene (PTFE, DuPont, Teflon 8A) in 8:1:1 ratio in mass inside an Ar-filled glovebox. The mixed composite was then rolled into free-standing thin films inside an Ar-filled glovebox. The total loading of the cathode composite was ≈26 mg cm^{-2}. The SiO_x-graphite electrode was fabricated at Argonne's Cell Analysis, Modeling and Prototyping (CAMP) Facility, and comprised 70 wt.% of SiO_x (Osaka), 16 wt.% MagE3 graphite (Hitachi), 1 wt.% single-walled carbon nanotubes (Tuball), 1 wt.% of carboxymethyl cellulose (CMC) and 12 wt.% of an acrylate binder (Battbond 290 S, Blue Ocean and Black Stone) pasted on a 10 µm copper foil. The CMC was present in the nanotube dispersion. Total anode coating loading was ≈3.18 mg cm^{-2}. For the full-cell testing, the N/P ratio was fixed to be 1.0 based on the first charge capacity of the cathode and the first discharge capacity of the anode.

In Situ and Ex Situ Characterization: In situ thermal XRD measurements were performed using a Bruker D8 Advance diffractometer with an Anton Paar HTK 1200 N oven chamber. To keep the required scan time low, diffraction data was collected between a limited range of 2q (10°–60°) using Cu Kα radiation. These scans were performed twice during each 10 min hold that occurred throughout the heating procedures. A rapid heating rate of 20° min^{-1} was employed between each set of scans to minimize downtime.

In situ-electrochemistry XRD analysis was conducted on a Bruker D8 ADVANCE X-ray diffractometer with Mo-Kα radiation. An in situ cell with a Be window was cycled at 5 mA g^{-1} between 4.5 and 2.5 V using a Maccor potentiostat. The XRD patterns were collected in the 2q ranging from 7° to 27° every 1 h at room temperature.

The O *K*-edge RIXS spectra were collected by the iRIXS endstation at beamline 8.0.1 at the Advanced Light Source, Lawrence Berkeley National Laboratory. A homemade transfer kit was used to transfer the species from the Ar-filled glovebox to the measurement chamber to avoid any air exposure to the samples. The RIXS spectra were continuously scanned through the O-*K* pre-edge region with the excitation energy step size of 0.2 eV and dwell time of 90 s. To minimize beam damage, the specimen was repeatedly moved up and down by 0.5 mm during measurement, and it was confirmed that the spectrum was well averaged due to the long dwell time. The collected O-*K* RIXS spectra were used to create 2D RIXS maps as functions of emission and excitation energies. Further processing, including normalization, cosmic ray removal, etc., has been conducted for the 2D map as used in the previous work.[52]

Operando X-ray absorption spectroscopy (XAS) measurements at the Mn K-edge were performed in transition mode at beamline 7-BM of the National Synchrotron Light Source II, Brookhaven National Laboratory. A Si (111) monochromator was used to select the incident beam energy. A Rh-coated mirror was applied to obtain harmonic rejection. For the ex situ samples, the cathode was prepared in the same way as described in the electrochemistry section and was charged to different SOCs in a coin cell. The cells were disassembled and the cathode films were washed in DEC solvent in an Ar-filled glovebox. To calibrate the energy, the spectra of Mn-metal foil was simultaneously measured. Normalization and calibration of raw data were performed by Athena software.[53]

Custom-built Swagelok cells were used as described previously.[54–56]The anode was 11-mm Li foil, and the cathode was a Li_6MnO_4 electrode. The separator was composed of one sheet of quartz fiber filter paper (Whatman QM-A) on the Li-metal side and one sheet of polypropylene (Celgard 2500) on the Li_6MnO_4 side. The electrolyte was 1 M lithium hexafluorophosphate ($LiPF_6$, BASF) in 1:1 (vol) mixture

of ethylene carbonate (EC, Gotion):dimethyl carbonate (DMC, Gotion), and the electrolyte loading was 60 µL cm^{-2}. After assembly in an Ar-filled glovebox, the hermetically sealed, custom-built Swagelok cells were appropriately attached to the DEMS apparatus to avoid air exposure. The custom-built DEMS instrument and its operation was described in previous publications.[54–56] The cells were cycled on a Bio-Logic VSP-series potentiostat under positive Ar pressure (≈1.2 bar). For all the DEMS experiments, each cell was charged at a constant current of 10 mA g^{-1} to an upper cut-off voltage of 4.5 V versus Li/Li^+ and subsequently held at the upper cutoff voltage for 5 h. After charging, the cell was discharged at a constant current of 10 mA g^{-1} to a lower cut-off voltage of 2.5 V versus Li/Li^+. Throughout the experiment, the cell headspace was purged with 500 µL of Ar by the DEMS instrument every 30 min, and any accumulated gases were swept to the mass spectrometer chamber for analysis. The apparatus was calibrated for O_2, CO_2, and H_2 in Ar, allowing for the determination of the partial pressures of each analyte. The amount of each gas evolved was then quantified using the known volume, temperature, and partial pressure of the gas in each sample using the ideal gas law.

A Kratos Axis Ultra fitted with a monochromated Aluminium source ($K\alpha$ = 1486.6 eV) was used for collecting the X-ray photoelectron spectra. Survey spectra were acquired employing a Pass Energy of 160 eV. High-resolution, core-level spectra for all elements were acquired with a Pass Energy of 20 eV. All spectra were referenced against the C1s peak at 284.5 eV to compensate for charging effects during acquisition.

Supporting Information

Supporting Information is available from the Wiley Online Library or from the author.

Acknowledgements

This work was funded by the LG Energy Solution BIC (Battery Innovative Contest) program of LG Energy Solution, Ltd. under Contract No. 20181787. This work was also supported by the Assistant Secretary for Energy Efficiency and Renewable Energy, Vehicle Technologies Office, of the U.S. Department of Energy under Contract DEAC02-05CH11231 (DRX+ program). This work was authored in part by UChicago Argonne, LLC, Operator of Argonne National Laboratory ("Argonne"). Argonne, a U.S. Department of Energy Office of Science laboratory, is operated under Contract No. DE-AC02–06CH11357. Soft X-ray experiments were performed at BL8.0.1 of the Advanced Light Source (ALS), a DOE Office of Science User Facility, under contract no. DE-AC02-05CH11231. This research used beamline 7-BM of the National Synchrotron Light Source II, a U.S. Department of Energy (DOE) Office of Science User Facility operated for the DOE Office of Science by Brookhaven National Laboratory under Contract No. DE-SC0012704.

Conflict of Interest

The authors declare no conflict of interest.

Author Contributions

H.K. and K.J. contributed equally to this work. H.K. performed conceptualization, investigation, visualization, supervision, acquired funding acquisition, and wrote the original Draft.; K.J. performed conceptualization, investigation, visualization, and wrote the original draft.; N.S., V.S.A., Z.C., M.C., and G.H.L. performed investigation, visualization, and wrote the original draft.; S.E.T. performed investigation; F.B. performed investigation and visualization; Y.W.B. and P.Z. performed investigation; D.L., B.P., and W.J. performed project administration; B.M. and W.Y. performed supervision. All authors reviewed and edited the final manuscript.

Data Availability Statement

The experiment data that support the findings of this study are available from the corresponding author upon reasonable request.

Keywords

additive, cathode, Li_6MnO_4, lithium, manganese oxide

Received: August 31, 2024
Revised: January 22, 2025
Published online: February 2, 2025

[1] H. Zhang, J. Cheng, H. Liu, D. Li, Z. Zeng, Y. Li, F. Ji, Y. Guo, Y. Wei, S. Zhang, T. Bai, X. Xu, R. Peng, J. Lu, L. Ci, *Adv. Energy Mater.* **2023**, *13*, https://doi.org/10.1002/aenm.202300466.
[2] W. Lee, Y. S. Byeon, S. Lee, S. Kong, M.-S. Park, W.-S. Yoon, *Adv. Energy Mater.* **2024** https://doi.org/10.1002/aenm.202304533.
[3] L. Jin, C. Shen, Q. Wu, A. Shellikeri, J. Zheng, C. Zhang, J. P. Zheng, *Adv. Sci.* **2021**, *8*, 2005031.
[4] F. Wang, B. Wang, J. Li, B. Wang, Y. Zhou, D. Wang, H. Liu, S. Dou, *ACS Nano* **2021**, *15*, 2197.
[5] H. Xu, S. Li, C. Zhang, X. Chen, W. Liu, Y. Zheng, Y. Xie, Y. Huang, J. Li, *Energy Environ. Sci.* **2019**, *12*, 2991.
[6] H. J. Kim, S. Choi, S. J. Lee, M. W. Seo, J. G. Lee, E. Deniz, Y. J. Lee, E. K. Kim, J. W. Choi, *Nano Lett.* **2016**, *16*, 282.
[7] J. Jang, I. Kang, J. Choi, H. Jeong, K.-W. Yi, J. Hong, M. Lee, *Angew. Chem., Int. Ed.* **2020**, *59*, 14473.
[8] M. Noh, J. Cho, *J. Electrochem Soc.* **2012**, *159*, A1329.
[9] X. Liu, Y. Tan, W. Wang, C. Li, Z. W. Seh, L. Wang, Y. Sun, *Nano Lett.* **2020**, *20*, 4558.
[10] J. Zhao, Z. Lu, N. Liu, H.-W. Lee, M. T. McDowell, Y. Cui, *Nat. Commun.* **2014**, *5*, 5088.
[11] Z. Wang, Y. Fu, Z. Zhang, S. Yuan, K. Amine, V. Battaglia, G. Liu, *J. Power Sources* **2014**, *260*, 57.
[12] W. Zhong, Z. Zeng, S. Cheng, J. Xie, *Adv. Funct. Mater.* **2024**, *34*, 2307860.
[13] M.-S. Park, Y.-G. Lim, S. M. Hwang, J. H. Kim, J.-S. Kim, S. X. Dou, J. Cho, Y.-J. Kim, *ChemSusChem* **2014**, *7*, 3138.
[14] C. Zhan, Z. Yao, J. Lu, L. Ma, V. A. Maroni, L. Li, E. Lee, E. E. Alp, T. Wu, J. Wen, Y. Ren, C. Johnson, M. M. Thackeray, M. K. Y. Chan, C. Wolverton, K. Amine, *Nat. Energy* **2017**, *2*, 963.
[15] C. S. Johnson, S.-H. Kang, J. T. Vaughey, S. V. Pol, M. Balasubramanian, M. M. Thackeray, *Chem. Mater.* **2010**, *22*, 1263.
[16] B. Zhu, N. Wen, J. Wang, Q. Wang, J. Zheng, Z. Zhang, *Chem. Sci.* **2024** https://doi.org/10.1039/d4sc03052d.
[17] B. Zhu, W. Zhang, Q. Wang, Y. Lai, J. Zheng, N. Wen, Z. Zhang, *Adv. Funct. Mater.* **2024**, *34*, https://doi.org/10.1002/adfm.202315010.
[18] D. Wang, J. Wang, X. Li, C. Han, H. Fei, Z. Wu, *J. Alloy. Compd.* **2024**, *992*, 174607.
[19] Y.-G. Lim, D. Kim, J.-M. Lim, J.-S. Kim, J.-S. Yu, Y.-J. Kim, D. Byun, M. Cho, K. Cho, M.-S. Park, *J. Mater. Chem. A* **2015**, *3*, 12377.
[20] S. Narukawa, *Solid State Ionics* **1999**, *122*, 59.
[21] K. Jun, L. Kaufman, W. Jung, B. Park, C. Jo, T. Yoo, D. Lee, B. Lee, B. D. McCloskey, H. Kim, G. Ceder, *Adv. Energy Mater.* **2023** https://doi.org/10.1002/aenm.202301132.
[22] Y. Guo, X. Li, Z. Wang, H. Guo, J. Wang, *J. Energy Chem.* **2020**, *47*, 38.
[23] K.-S. Park, D. Im, A. Benayad, A. Dylla, K. J. Stevenson, J. B. Goodenough, *Chem. Mater.* **2012**, *24*, 2673.
[24] J. Ma, Y.-N. Zhou, Y. Gao, X. Yu, Q. Kong, L. Gu, Z. Wang, X.-Q. Yang, L. Chen, *Chem. Mater.* **2014**, *26*, 3256.

[25] T. Kim, J. Lee, M. J. You, C. H. Song, S.-M. Oh, J. Moon, J. H. Kim, M.-S. Park, *ACS Appl. Mater. Interfaces* **2023**, *15*, 18790.
[26] G. Vitins, E. A. Raekelboom, M. T. Weller, J. R. Owen, *J. Power Sources* **2003**, *119*, 938.
[27] M. G. Kim, J. Cho, *J. Mater. Chem.* **2008**, *18*, 5880.
[28] C. K. Back, R.-Z. Yin, S.-J. Shin, Y.-S. Lee, W. Choi, Y.-S. Kim, *J. Electrochem. Soc.* **2012**, *159*, A887.
[29] H. Park, T. Yoon, Y.-U. Kim, J. H. Ryu, S. M. Oh, *Electrochim. Acta* **2013**, *108*, 591.
[30] Y. Wu, W. Zhang, S. Li, N. Wen, J. Zheng, L. Zhang, Z. Zhang, Y. Lai, *ACS Sustainable Chem. Eng.* **2023**, *11*, 1044.
[31] W. Sun, S. T. Dacek, S. P. Ong, G. Hautier, A. Jain, W. D. Richards, A. C. Gamst, K. A. Persson, G. Ceder, *Sci. Adv.* **2016**, *2*, 1600225.
[32] N. J. Szymanski, Y. Zeng, T. Bennett, S. Patil, J. K. Keum, E. C. Self, J. Bai, Z. Cai, R. Giovine, B. Ouyang, F. Wang, C. J. Bartel, R. J. Clément, W. Tong, J. Nanda, G. Ceder, *Chem. Mater.* **2022**, *34*, 7015.
[33] L. Cui, X. Li, Z. Wang, W. Peng, J. Wang, G. Yan, H. Duan, G. Li, X. Zhou, H. Guo, *J. Alloy. Compd.* **2025**, *1010*, 177976.
[34] K. Luo, M. R. Roberts, N. Guerrini, N. Tapia-Ruiz, R. Hao, F. Massel, D. M. Pickup, S. Ramos, Y.-S. Liu, J. Guo, A. V. Chadwick, L. C. Duda, P. G. Bruce, *J. Am. Chem. Soc.* **2016**, *138*, 11211.
[35] M. Sathiya, G. Rousse, K. Ramesha, C. P. Laisa, H. Vezin, M. T. Sougrati, M.-L. Doublet, D. Foix, D. Gonbeau, W. Walker, A. S. Prakash, M. Ben Hassine, L. Dupont, J.-M. Tarascon, *Nat. Mater.* **2013**, *12*, 827.
[36] Z. Zhuo, C. D. Pemmaraju, J. Vinson, C. Jia, B. Moritz, I. Lee, S. Sallies, Q. Li, J. Wu, K. Dai, Y.-D. Chuang, Z. Hussain, F. Pan, T. P. Devereaux, W. Yang, *J. Phys. Chem. Lett.* **2018**, *9*, 6378.
[37] T.-Y. Huang, Z. Cai, M. J. Crafton, R. Giovine, A. Patterson, H.-M. Hau, J. Rastinejad, B. L. D. Rinkel, R. J. Clément, G. Ceder, B. D. McCloskey, *Chem. Mater.* **2024**, *36*, 6535.
[38] M. J. Crafton, T.-Y. Huang, Y. Yue, R. Giovine, V. C. Wu, C. Dun, J. J. Urban, R. J. Clément, W. Tong, B. D. McCloskey, *ACS Appl. Mater. Interfaces* **2023**, *15*, 18747.
[39] J. Si, R. Ma, Y. Wu, Y. Dong, K. Yao, *J. Mater. Sci.* **2022**, *57*, 8154.
[40] R. A. House, U. Maitra, L. Jin, J. G. Lozano, J. W. Somerville, N. H. Rees, A. J. Naylor, L. C. Duda, F. Massel, A. V. Chadwick, S. Ramos, D. M. Pickup, D. E. McNally, X. Lu, T. Schmitt, M. R. Roberts, P. G. Bruce, *Chem. Mater.* **2019**, *31*, 3293.
[41] G. Lee, V. W. Lau, W. Yang, Y. Kang, *Adv. Energy Mater.* **2021**, *11*, 2003227.
[42] D. Cao, X. Liu, X. Yuan, F. Yu, Y. Chen, *ACS Appl. Mater. Interfaces* **2021**, *13*, 39341.
[43] J. P. Perdew, K. Burke, M. Ernzerhof, *Phys. Rev. Lett.* **1996**, *77*, 3865.
[44] G. Kresse, J. Furthmüller, *Phys. Rev. B* **1996**, *54*, 11169.
[45] P. P. Ewald, *Ann Phys.-berlin* **1921**, *369*, 253.
[46] A. Jain, G. Hautier, S. P. Ong, C. J. Moore, C. C. Fischer, K. A. Persson, G. Ceder, *Phys. Rev. B* **2011**, *84*, 045115.
[47] X. Zhang, M. H. F. Sluiter, *J. Phase Equilibria Diffus.* **2016**, *37*, 44.
[48] P. Zhong, T. Chen, L. Barroso-Luque, F. Xie, G. Ceder, *Phys. Rev. B* **2022**, *106*, 024203.
[49] L. Barroso-Luque, P. Zhong, J. H. Yang, F. Xie, T. Chen, B. Ouyang, G. Ceder, *Phys. Rev. B* **2022**, *106*, 144202.
[50] L. Barroso-Luque, J. H. Yang, F. Xie, T. Chen, R. L. Kam, Z. Jadidi, P. Zhong, G. Ceder, *J. Open Source Softw.* **2022**, *7*, 4504.
[51] S. P. Ong, W. D. Richards, A. Jain, G. Hautier, M. Kocher, S. Cholia, D. Gunter, V. L. Chevrier, K. A. Persson, G. Ceder, *Comp. Mater. Sci.* **2013**, *68*, 314.
[52] G.-H. Lee, J. Wu, D. Kim, K. Cho, M. Cho, W. Yang, Y.-M. Kang, *Angew. Chem., Int. Ed.* **2020**, *59*, 8681.
[53] B. Ravel, M. A. Newville, *J. Synchrotron Radiat.* **2005**, *12*, 537.
[54] B. D. McCloskey, A. Speidel, R. Scheffler, D. C. Miller, V. Viswanathan, J. S. Hummelshøj, J. K. Nørskov, A. C. Luntz, *J. Phys. Chem. Lett.* **2012**, *3*, 997.
[55] B. D. McCloskey, A. Valery, A. C. Luntz, S. R. Gowda, G. M. Wallraff, J. M. Garcia, T. Mori, L. E. Krupp, *J. Phys. Chem. Lett.* **2013**, *4*, 2989.
[56] B. D. McCloskey, D. S. Bethune, R. M. Shelby, G. Girishkumar, A. C. Luntz, *J. Phys. Chem. Lett.* **2011**, *2*, 1161.